





Unveiling disparities and promises of Cu and Ag chalcopyrites for thermoelectrics

Han-Pu Liang ¹, Songyuan Geng,¹ Tiantian Jia,² Chuan-Nan Li ^{3,1}, Xun Xu,¹ Xie Zhang ^{4,*} and Su-Huai Wei ^{1,†}

¹Beijing Computational Science Research Center, Beijing 100193, China

²School of Science, Nanjing University of Posts and Telecommunications, Nanjing 210046, China

³Department of Physics, University of Science and Technology of China, Hefei 230026, China

⁴School of Materials Science and Engineering, Northwestern Polytechnical University, Xi'an 710072, China



(Received 12 September 2023; revised 10 December 2023; accepted 9 January 2024; published 24 January 2024)

Cu chalcopyrites exhibit excellent thermoelectric performance because of their high thermopower and low thermal conductivity. Conversely, despite that Ag chalcopyrites have even lower thermal conductivity than the Cu-based ones, they generally display lower thermoelectric performance. The underlying physics for the thermoelectric disparity between Cu- and Ag-based materials remains unclear. In this work we investigate thermal transport and thermopower of ternary $AMSe_2$ chalcopyrites ($A=Cu/Ag$; $M=Ga/In$) using first-principles methods. We reveal that strong anharmonicity from $s-d$ coupling leads to low thermal conductivity in Cu as well as Ag chalcopyrites, whereas weaker bond strength and heavier atomic mass contribute to even lower thermal conductivity in Ag chalcopyrites than the Cu ones. On the other hand, Cu chalcopyrites show superior thermopower owing to their higher band degeneracy and stronger $p-d$ coupling, which leads to enhanced mobility. We conclude that if Ag chalcopyrites could reach comparable hole concentrations as in Cu chalcopyrites, high thermoelectric performance in Ag chalcopyrites can also be achieved because of their low thermal conductivity. Understanding the disparity between Cu and Ag chalcogenides from a mechanistic perspective is important for future design of superior thermoelectric materials.

DOI: [10.1103/PhysRevB.109.035205](https://doi.org/10.1103/PhysRevB.109.035205)

I. INTRODUCTION

Thermoelectric materials possess a unique capability to convert heat directly into electricity, making them an important component of global sustainable energy solutions. By harnessing otherwise wasted heat, they offer significant potential for energy recovery [1–7]. To improve their thermoelectric performance, it is crucial to reduce the thermal transport coefficient κ and enhance the thermopower factor $PF = S^2\sigma$, where S and σ are the Seebeck coefficient and electrical conductivity, respectively, as represented by the thermoelectric figure of merit $zT = S^2\sigma T/\kappa$ [8]. To reduce thermal transport, traditional approaches employ heavier atoms to reduce phonon velocities or increase anharmonicity in atomic displacement to enhance phonon scattering [9,10]. To enhance the thermopower factor, materials with large valley degeneracies are favored because they could have high variation of the density of states (DOS) at the Fermi surface to enhance the Seebeck coefficient while maintaining the carrier mobility [11,12]. These strategies have guided the discovery of novel materials like PbTe-AgSbTe₂ [13], Cu₂(S, Se, Te) [14,15], and FeNbSb-based half-Heusler alloys for thermoelectric applications [16].

Chalcopyrite semiconductors AMX_2 ($A=Cu/Ag$; $M=Ga/In$; $X=S/Se/Te$) and their solid solutions have garnered considerable interest owing to their remarkable properties for energy-related applications [17–19]. Among

these materials, the Cu chalcopyrites exhibit exceptional thermoelectric performance, attributable to their low thermal conductivity and high power factor. Notably, the Ag chalcopyrites exhibit even lower thermal conductivity than the Cu-based ones [20], but, generally, their thermoelectric performance is lower than their Cu counterparts [21–23]. Experiments [24] show that, in $ABTe_2$ compounds ($A=Cu/Ag$; $B=Ga/In$), native A -site vacancies are the origin of the distinct electrical conductivity. Meanwhile, in Ag and Cu chalcopyrites, the vibrations of Ag-Te clusters and Te atoms lead to significant differences in the thermal conductivity, respectively. However, it is still unclear what the underlying mechanism accounting for the electronic and phonon differences between Cu- and Ag-based materials is and whether Ag chalcopyrite could have better thermoelectric performance than Cu chalcopyrites since the former has lower thermoelectricity. Understanding these differences and finding the root reasons are important for future design of superior thermoelectric materials.

In this work we explore the disparity of thermoelectric properties between Cu- and Ag-based $AMSe_2$ chalcopyrite compounds ($A=Cu/Ag$; $M=Ga/In$). We reveal that the low lattice thermal conductivity of Cu and Ag chalcopyrites can be attributed to the strong $s-d$ coupling in these compounds, which leads to large anharmonicity and strong phonon scattering. Furthermore, Ag chalcopyrites have weaker bonds and heavier atomic mass, and thus lower phonon frequency, which explains the even lower thermal conductivity in Ag-based materials than that in Cu-based materials. Concerning thermopower, Cu chalcopyrites exhibit superior Seebeck coefficients and electrical conductivity than the Ag counterparts

*xie.zhang@nwpu.edu.cn

†suhuaiwei@csrc.ac.cn

TABLE I. Structural, electronic, and thermoelectric parameters of $AMSe_2$ compounds, including the lattice constants a and c , tetragonal distortion η , internal distortion u , crystal-field splitting Δ_{CF} , lattice thermal conductivity κ_L , thermopower factor PF , and figure of merit zT of p type. PF and zT are listed at 700 K. κ_L is measured at 300 K. Hole concentration is chosen to be 10^{19} cm^{-3} . Values in brackets are experimental data from Refs. [25–30].

Structure	a (Å)	c (Å)	η	u	Δ_{CF} (eV)	κ_L ($\text{W m}^{-1} \text{K}^{-1}$)	PF ($\mu\text{W m}^{-1} \text{K}^{-1}$)	zT
CuGaSe ₂	5.64 (5.61)	11.08 (11.00)	0.98 (0.98)	0.251	-0.11 (-0.12)	3.98 (4.20)	827	0.22
CuInSe ₂	5.82 (5.78)	11.70 (11.55)	1.00 (1.00)	0.228	0.00 (0.01)	3.34 (2.90)	1229	0.39
AgGaSe ₂	6.02 (5.98)	11.02 (10.88)	0.92 (0.91)	0.284	-0.24 (-0.25)	0.84 (1.10)	291	0.46
AgInSe ₂	6.16 (6.07)	11.88 (11.69)	0.96 (0.96)	0.261	-0.14 (-0.12)	0.86	370	0.53

due to their high band degeneracy and strong $p-d$ coupling. We find that Ag chalcopyrites could possess an advantage for the thermoelectric performance owing to their lower thermal conductivity. However, the poor hole dopability, which is intrinsic to the Ag chalcogenides, limits the thermoelectric performance of Ag chalcopyrites, consistent with experimental observations. These understandings provide valuable guidelines for future design of better thermoelectric materials.

II. COMPUTATIONAL METHODS

Our first-principles calculations were performed within the density functional theory [31,32] as implemented in the Vienna *ab initio* simulation package (VASP) [33–35] using projector augmented-wave pseudopotentials [36,37]. The plane-wave energy cutoff is set to 550 eV. The Monkhorst-Pack scheme was used to sample the Brillouin zone, and a k -point mesh of $8 \times 8 \times 8$ was used for the calculations. The structural optimizations and electronic band structures were calculated by using the Heyd-Scuseria-Ernzerhof (HSE) [38] hybrid functional with the fraction of nonlocal Fock exchange set to 0.3. The phonon dispersions and the second-order interatomic force constants (IFCs) were calculated using the PHONOPY package [39]. The third-order IFCs and the lattice thermal conductivity were evaluated by employing the SHENGBTE code [40]. The fourth-order IFCs, controlling the four-phonon scattering rates, were calculated by the FOURPHONON package [41]. The second-, third-, and fourth-order IFCs are evaluated using the $4 \times 4 \times 4$, $3 \times 3 \times 2$, and $2 \times 2 \times 2$ supercells, respectively, with a Γ -centered k -point mesh of $1 \times 1 \times 1$. Electronic transport properties were calculated by solving the semiclassical Boltzmann transport equation in the AMSET code [42–44]. To compare thermal properties of different materials on an equal footing, the carrier concentration was chosen to be 10^{19} cm^{-3} .

III. RESULTS AND DISCUSSION

A. Crystal structure and the tetragonal distortion

Ternary $AMSe_2$ compounds adopt the stable chalcopyrite (CH) structure, which contains Se-centered A_2M_2 local tetrahedron clusters [25,45]. The orientations of the A -Se- M tetrahedra lie along the a or b axis, as depicted in Fig. 1(a). Table I presents the calculated structural parameters for these compounds. The internal distortion parameter $u = 1/4 + (r_{A-Se}^2 - r_{M-Se}^2)/a^2$ and the tetragonal distortion parameter $\eta = c/2a$ both reflect the structural distortion of the chalcopyrite structure, where r_{A-Se} and r_{M-Se} are the

corresponding bond lengths. The tetragonal distortion in $AMSe_2$ materials is strongly influenced by the competition between the A -Se and M -Se bond lengths and bond strengths, as well as their orientations. The standard tetrahedron has equal edges and angles, i.e., $a = b$, $\eta = 1$, and $\theta_{\text{std}} = 109.47^\circ$. Tetragonal distortion arises when the Se atom bonds with two nonequivalent atoms, i.e., a group-I A atom and a group-III M atom, breaking the symmetry, and varies with the change of element [see Fig. 1(b)].

The high number of valence states of the M atom results in a strong, more covalent M -Se bond, which controls the distortion of the A -Se- M tetrahedron, i.e., the M -Se- M angle tends to maintain the standard tetrahedral angle of 109.47° (having a large bond-bending force constant), while the weak, more ionic A -Se- A angle is more easy to deform (having small

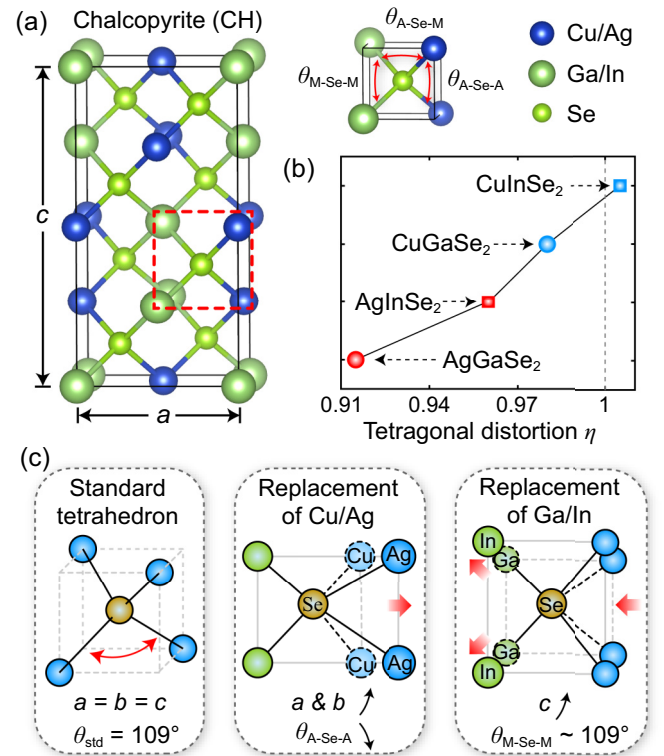


FIG. 1. (a) Crystal structure and its tetrahedron in the CH structure. The A -Se- M orientation is along the a or b axis. (b) Tetragonal distortion η of chalcopyrite $AMSe_2$ compounds. (c) Schematic diagrams of a standard tetrahedron and the lattice difference induced by Cu/Ag and Ga/In replacements.

bond-bending force constant), as illustrated in Fig. 1(c). In the CH structure, when the group-I A atom changes from Cu to Ag, the M -Se- M angle is kept as close to θ_{std} as possible, so the c axis is almost maintained. The longer Ag-Se bond tends to increase the size along the a and b axes and reduces the Ag-Se-Ag bond angle, resulting in a decreased η . In contrast, when the Ga atom is replaced by an In atom, the In-Se bond expands the c axis and enlarges the A-Se-A angle, causing an increase in η . Therefore materials with similar bond lengths between A-Se and M-Se exhibit more ideal tetrahedron with $\eta \sim 1$. When the A atom size increases, η decreases. When the M atom size increases, η increases. Cu-based materials have η that is close to 1, and when Cu is replaced by Ag, the Ag-based materials have much smaller η , as seen in Table I and Fig. 1(b). $\eta < 1$ will lead to a negative crystal-field splitting at the valence band edge of the chalcopyrite compounds (see Table I), which will significantly reduce the density of states of the p -type chalcopyrite semiconductors and affect the thermoelectric properties, as will be discussed below.

B. Difference in thermal transport between Cu- and Ag-based chalcogenides

Lattice anharmonicity is a key factor that reduces lattice thermal conductivity in complex structures. Symmetry-controlled s - d coupling can induce strong anharmonicity, enhancing phonon scattering, because it pushes the occupied d orbital down in energy, substantially lowering the lattice vibrational potential energy curve [46–48]. For example, the remarkably low lattice thermal conductivity of Cu-based materials is attributed to the strong s - d coupling, as the Cu atom possesses the highest fully occupied d orbital energy and smallest s - d energy separation in all elements. As a comparison, we compare the lattice vibrational potential energy curve and the anharmonicity of ZnSe with that of CuGaSe₂ in Fig. 2. For ZnSe the occupied Zn 3d energy level is much deeper inside the valence band, and thus the s - d coupling is much weaker and the vibrational potential energy curve is more harmonic. On the other hand, due to the strong s - d coupling, when the Cu atom moves away from the high-symmetry position, CuGaSe₂ presents more flat energy curves compared to ZnSe, thus creating more phonon anharmonicity. Similar comparisons are shown between CdSe and AgInSe₂. However, despite the Ag atoms having a deeper d orbital than Cu, due to the relatively weaker s - d coupling induced anharmonicity, it does not result in an increased potential energy curve. This is because the larger atomic size of Ag weakens the Ag-Se bond strength, thereby reducing the overall energy. A similar energy trend is observed when comparing ZnSe with CdSe. Furthermore, in Cu and Ag chalcopyrites without inversion symmetry, the s - d coupling mainly induces third-order anharmonicity. Thus the self-consistent phonon method, which considers quartic anharmonicity, is less important on the renormalized phonon dispersion, as seen in Fig. S1 in the Supplemental Material (hereafter SM) [49].

Lattice thermal conductivity can be derived in detail from the phonon properties, i.e., $\kappa_L = \sum_{\lambda} c_v v_{\lambda}^2 \tau_{\lambda}$, where c_v is the unit heat capacity, v_{λ} is the phonon group velocity, and τ_{λ} is the phonon relaxation time, which is inverse to the

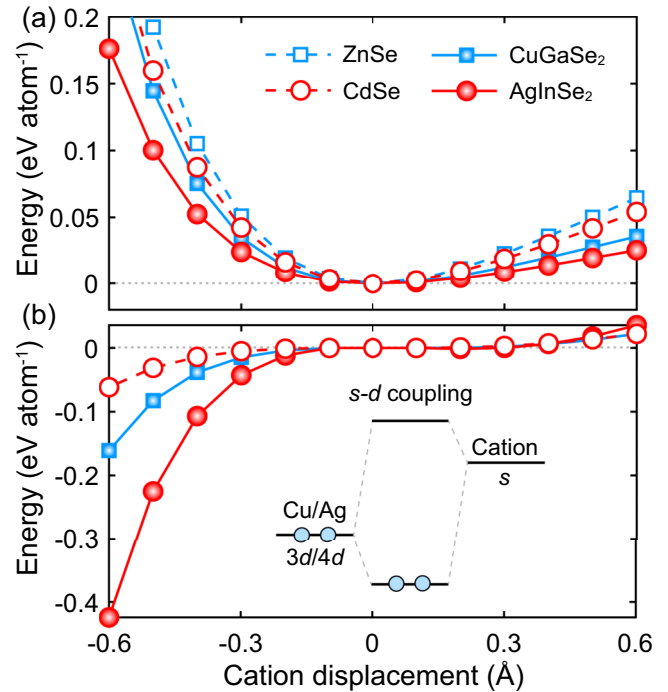


FIG. 2. (a) Potential energy curves as a function of atomic displacement, where the potential energies at equilibrium are set as zero for comparison. (b) The energy difference $\Delta E = E_{\text{calc}} - E_{\text{harm}}$, where E_{calc} is the calculated energy curve, and E_{harm} is the second-order fitting energy curve. We displaced cation of Zn, Cd, Cu, and Ag along the bond stretching direction in ZnSe, CdSe, CuGaSe₂, and AgInSe₂. The inset shows the band coupling between the s and d orbitals schematically.

phonon-scattering rates. Here we consider the thermal conductivity concluding three- and four-phonon scattering rates, as seen in Fig. S2 in the SM [49]. Higher phonon velocities and less phonon scattering result in more rapid heat conduction. The thermal conductivity is mainly controlled by phonon frequency: lower frequencies lead to reduced velocities and thus suppressed thermal conductivity. As illustrated in Fig. 3(a), thermal conductivities of $AM\text{Se}_2$ compounds follow a linear relationship with the frequencies of lowest-energy optical phonons. Cu-based chalcopyrites exhibit significantly higher thermal conductivities than the Ag-based ones, because of the higher frequency from the lighter Cu atom. Furthermore, in Cu-based compounds, from CuGaSe₂ to CuInSe₂, the increasing group-III atomic mass drops the phonon frequency and reduces the thermal conductivity, because the group-III atoms dominate the low-energy phonons. In contrast, in Ag-based compounds, from AgGaSe₂ to AgInSe₂, an unexpected rise in phonon frequency and thermal conductivity is observed. This can be attributed to the larger mass of Ag, which minimizes the impact of variations in group-III atomic mass. Instead, the tetragonal distortion η becomes a more dominant factor. The increase of η from AgGaSe₂ to AgInSe₂ leads to increased phonon frequencies and thus increased thermal conductivity, as will be discussed below.

To intuitively explore the relationship between tetragonal distortion and phonon frequency, we consider the bond-bending motion of A-centered tetrahedron, which is

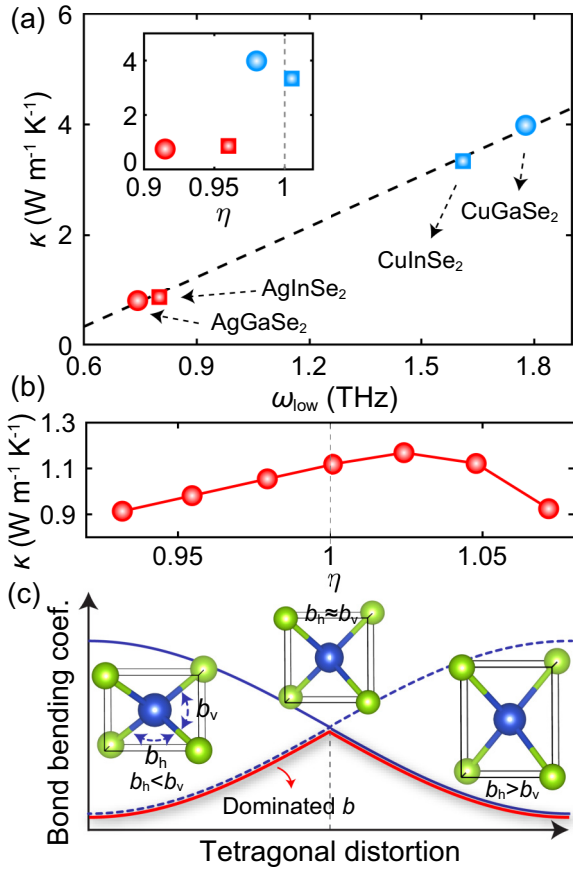


FIG. 3. (a) Thermal conductivity κ vs the frequencies of the lowest-energy optical phonons and tetragonal distortion η (the inset) for $AMSe_2$. (b) κ varies with η in $AgGaSe_2$, and (c) the schematic diagram of bond-bending coefficient k vs η in A-centered tetrahedron. The calculations are performed at 300 K.

dominated by the low-energy phonons. When $\eta_{\text{tetra}} = c_{\text{tetra}}/a_{\text{tetra}} < 1$, the horizontal and vertical Se-A-Se angles, θ_h and θ_v , deviate from the ideal angle. This leads to weaker bond-bending strength along the horizontal direction than the vertical direction, i.e., $b_h < b_v$, due to the angle asymmetry of the bond-bending force, causing the low-energy phonon frequency to be dominated by b_h . As η_{tetra} approaches 1, the angles of the tetrahedron become close to the ideal values, forming a standard tetrahedron. This causes the bond-bending coefficients $b_h = b_v$, resulting in the low-energy phonon frequency reaching a peak. As η_{tetra} continues to increase, b_v dominates the low-energy phonon behavior and lowers the frequency. As a result, the thermal conductivity rises and then drops with increasing η . Therefore, from $AgGaSe_2$ to $AgInSe_2$, the increased η leads to an increased thermal conductivity. Figure 3(b) plots the thermal conductivity as a function of η for $AgGaSe_2$, showing that the thermal conductivity reaches its maximum at around $\eta = 1$, confirming our analysis and expectation.

To quantitatively show the difference in thermal conductivity, Fig. 4(a) shows the phonon group velocities and scattering rates on the phonon spectra, in the case of $CuGaSe_2$ and $AgGaSe_2$. Due to the greater mass of the Ag atom, the low-energy phonons in $AgGaSe_2$ downshift compared to

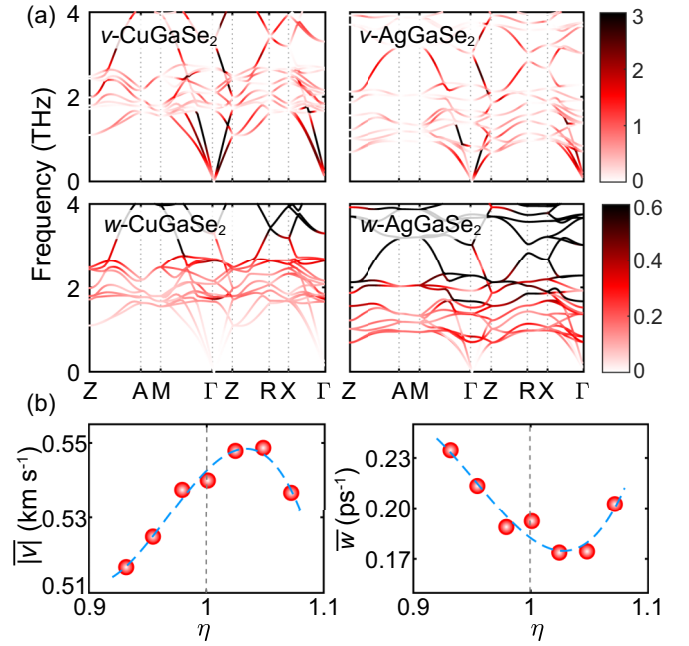


FIG. 4. (a) Phonon group velocities v (km s⁻¹) and phonon-scattering rates w (ps⁻¹) and distribution on the phonon spectra of $CuGaSe_2$ and $AgGaSe_2$. (b) Averaged $|\bar{v}|$ and \bar{w} varies with η in $AgGaSe_2$. The average data is calculated from the frequency range of 0–2 THz [49].

those in $CuGaSe_2$. This results in increased three-phonon scattering between low-energy optical phonons and acoustic phonons, as well as a soft acoustic phonon. These factors enhance phonon-scattering rates and decrease the phonon group velocity in $AgGaSe_2$. Figure 4(b) illustrates the averaged phonon group velocities and scattering rates as a function of η . As η increases, the phonon group velocities first rise and then drop, whereas the phonon-scattering rates first decrease and then increase. Both metrics exhibit a peak at around $\eta \sim 1.05$, aligning with the trend of thermal conductivity with respect to η .

C. Difference in thermoelectricity between Cu- and Ag-based chalcogenides

In the following we will compare the thermoelectric properties of Cu vs Ag compounds in terms of power factor PF , which is proportional to the product of the Seebeck coefficient S^2 and the electrical conductivity σ .

Chalcopyrites typically feature noncubic tetragonal structures with distorted tetrahedra. This distortion, due to the crystal-field effect, splits the triply degenerate valence band Γ_{15v} state into a nondegenerate band Γ_{4v} and a doubly degenerate band Γ_{5v} (for simplicity we use single group representation in this work). The crystal-field splitting $\Delta_{CF} = E(\Gamma_{5v}) - E(\Gamma_{4v})$ linearly correlates with the tetragonal distortion η [21]. Figures 5(a)–5(d) show the electronic structures of the $AMSe_2$ compounds. The calculated band gaps and Δ_{CF} are consistent with the experimental values (Tables I and II). Generally, high degeneracy, i.e., small Δ_{CF} , can result in a sharp DOS peak at the Fermi surface to enhance the Seebeck coefficient while possibly maintaining the carrier

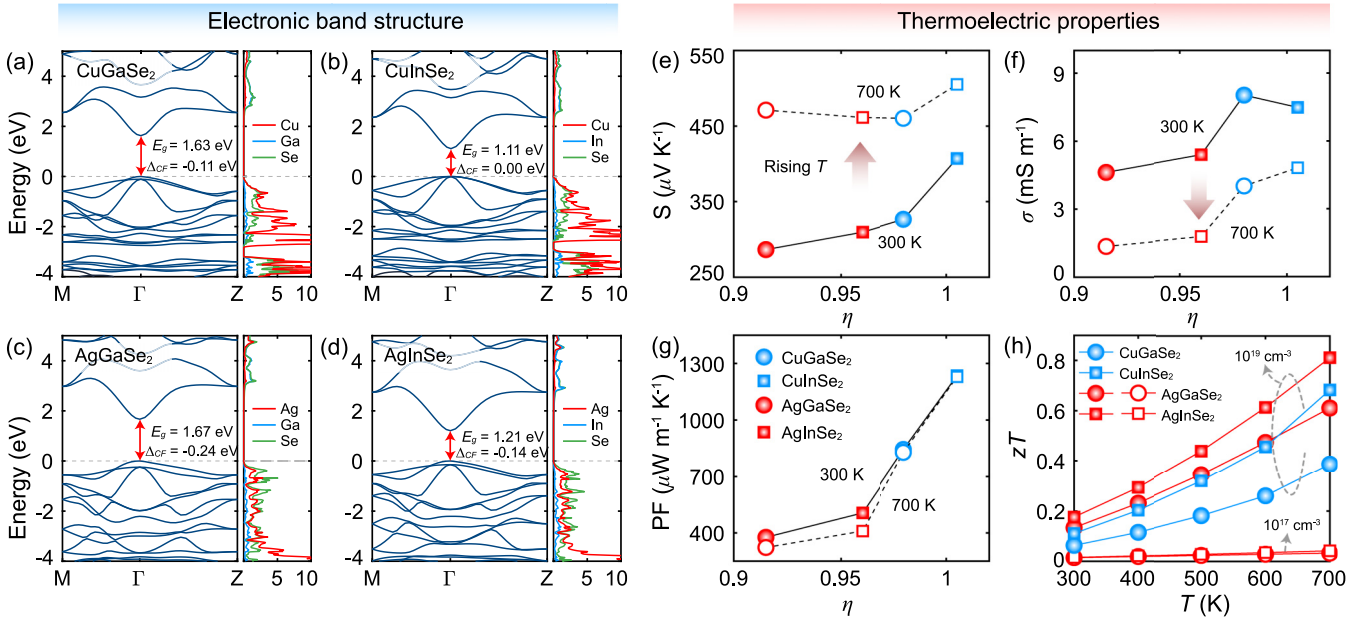


FIG. 5. Band structures and its density of states for (a) CuGaSe₂, (b) CuInSe₂, (c) AgGaSe₂, and (d) AgInSe₂. (e) Seebeck coefficient S , (f) electrical conductivity σ , and (g) power factor PF vs tetragonal distortion η at 300 and 700 K for $AMSe_2$ compounds. (h) Figure of merit zT vs temperature T . Filled and unfilled markers denote zT at the hole concentration of 10^{19} cm^{-3} and 10^{17} cm^{-3} , respectively.

mobility [8,50]. Figure 5(e) illustrates the difference of Seebeck coefficient between Cu and Ag chalcopyrites, revealing that the Seebeck coefficient peaks when η approaches 1, which is a common phenomenon of tetragonal chalcopyrites. Thus Cu chalcopyrites exhibit higher S due to the small deviation of η from 1, in contrast with the Ag compounds.

It is interesting to see the effect of temperature on the Seebeck coefficient for these materials in Fig. 5(e). As discussed above, crystal-field splitting plays a dominant role in determining the Seebeck coefficient; therefore CuInSe₂ with the η closest to 1 exhibits the highest Seebeck coefficient at 300 K due to its negligible crystal-field splitting. At 700 K the Fermi distribution broadens, making the crystal-field splitting easier to overcome [8], thus enhancing the Seebeck coefficient, especially for Ag-based compounds, therefore reducing the difference on the Seebeck coefficient between the Cu and Ag compounds.

On the other hand, the strong p - d coupling in Cu chalcopyrites leads to a smaller effective mass for Cu-based chalcogenides than for the Ag-based ones (see Table II). Small effective mass at the valence band maximum (VBM) results in a large hole mobility of the Cu chalcopyrites, which leads to

TABLE II. Band gaps and hole effective masses at VBM along xy and z direction of $AMSe_2$ system. Values in brackets are experimental data from Refs. [25,27].

Structure	E_g (eV)	m_{xy}^* (m_0)	m_z^* (m_0)
CuGaSe ₂	1.63 (1.69)	0.58	2.82
CuInSe ₂	1.11 (1.01)	0.59	1.42
AgGaSe ₂	1.67 (1.81)	0.60	3.71
AgInSe ₂	1.21 (1.24)	0.63	4.25

superior electrical conductivity than the Ag ones, as illustrated in Fig. 5(f). As the temperature increases, electrical conductivity decreases, because the temperature enhances the carrier scattering, which impedes the mobility (see Fig. S4 in the SM [49]). By combining these effects, as seen in Fig. 5(g), the superior thermopower factor in Cu chalcopyrites compared to the Ag ones arises from the high band degeneracy and strong p - d coupling, which results in the large Seebeck coefficient and electrical conductivity.

Figure 5(h) plots the thermoelectric figure of merit zT vs temperature T for Cu- and Ag-based chalcopyrites. Despite that Cu chalcopyrites exhibit superior electrical properties, considering thermal transport, Ag chalcopyrites yield a better zT . At a high hole concentration of 10^{19} cm^{-3} , AgInSe₂ reaches a zT of 0.53 at 700 K, surpassing the theoretical value of 0.39 (the reported experimental value is 0.40 [21]) for CuInSe₂. However, achieving such high hole concentrations in Ag chalcopyrites is challenging due to the low occupied d orbital of Ag and the weak p - d coupling, which lowers the VBM of the Ag compounds, making it difficult to be doped p type [30]. At a low hole concentrations of 10^{17} cm^{-3} , the zT of AgInSe₂ is merely 0.03. This could explain why Ag chalcopyrites do not show experimentally superior thermoelectric properties to Cu chalcopyrites. If the hole concentrations in Ag chalcopyrites could be increased, their lower thermal conductivity would render them more advantageous in thermoelectric performance than their Cu counterparts.

IV. CONCLUSIONS

In summary, we explore the thermoelectric disparity between Cu and Ag chalcopyrites in $AMSe_2$ systems ($A = \text{Cu/Ag}$; $M = \text{Ga/In}$). We reveal that the low lattice thermal conductivity in both Cu and Ag chalcopyrites can be attributed

to the large anharmonicity from strong $s-d$ coupling. The Cu chalcopyrites exhibit notably higher thermal conductivities than their Ag counterparts because of the lighter Cu atom and because they have a tetragonal distortion parameter η is close to 1. We note that the origin of this tetragonal distortion in chalcopyrites stems from the imbalance between the weak A -Se and stronger M -Se bonds. On the other hand, Cu chalcopyrites show superior thermopower due to their higher band degeneracy and strong $p-d$ coupling. We conclude that the poor hole dopability limits the thermoelectric performance of Ag chalcopyrites. If the hole concentrations

in Ag chalcopyrites could be increased, their lower thermal conductivity would make them more advantageous in thermoelectric performance than their Cu counterparts.

ACKNOWLEDGMENTS

This work was supported by the National Natural Science Foundation of China (Grants No. 11991060, No. 12088101, No. 52172136, No. 12104035, and No. U2230402). We acknowledge computational resources from the Beijing Computational Science Research Center.

-
- [1] J. P. Heremans, V. Jovovic, E. S. Toberer, A. Sarmat, K. Kurosaki, A. Charoenphakdee, S. Yamanaka, and G. J. Snyder, *Science* **321**, 554 (2008).
- [2] G. J. Snyder and E. S. Toberer, *Nat. Mater.* **7**, 105 (2008).
- [3] H. Liang and Y. Duan, *Nanoscale* **13**, 11994 (2021).
- [4] T. Jia, J. Carrete, G. K. H. Madsen, Y. Zhang, and S.-H. Wei, *Phys. Rev. B* **105**, 245203 (2022).
- [5] T. Jia, X. Liu, Y. Zhang, and S.-H. Wei, *Phys. Rev. B* **107**, 115204 (2023).
- [6] C.-N. Li, H.-P. Liang, X. Zhang, Z. Lin, and S.-H. Wei, *npj Comput. Mater.* **9**, 176 (2023).
- [7] C. Qiu, Y. Song, H.-X. Deng, and S.-H. Wei, *J. Am. Chem. Soc.* **145**, 24952 (2023).
- [8] Y. Pei, X. Shi, A. LaLonde, H. Wang, L. Chen, and G. J. Snyder, *Nature (London)* **473**, 66 (2011).
- [9] H. Liang, H. Zhong, S. Huang, and Y. Duan, *J. Phys. Chem. Lett.* **12**, 10975 (2021).
- [10] F. Lv, H. Liang, and Y. Duan, *Phys. Rev. B* **107**, 045422 (2023).
- [11] Z. M. Gibbs, F. Ricci, G. Li, H. Zhu, K. Persson, G. Ceder, G. Hautier, A. Jain, and G. J. Snyder, *npj Comput. Mater.* **3**, 8 (2017).
- [12] W. Liu, X. Tan, K. Yin, H. Liu, X. Tang, J. Shi, Q. Zhang, and C. Uher, *Phys. Rev. Lett.* **108**, 166601 (2012).
- [13] M. Zhou, J.-F. Li, and T. Kita, *J. Am. Chem. Soc.* **130**, 4527 (2008).
- [14] Y. He, P. Lu, X. Shi, F. Xu, T. Zhang, G. J. Snyder, C. Uher, and L. Chen, *Adv. Mater.* **27**, 3639 (2015).
- [15] R. Zhou, H. Liang, Y. Duan, and S.-H. Wei, *J. Phys. Chem. Lett.* **14**, 737 (2023).
- [16] C. Fu, S. Bai, Y. Liu, Y. Tang, L. Chen, X. Zhao, and T. Zhu, *Nat. Commun.* **6**, 8144 (2015).
- [17] Y. Zhang, X. Yuan, X. Sun, B.-C. Shih, P. Zhang, and W. Zhang, *Phys. Rev. B* **84**, 075127 (2011).
- [18] Y. Hu, C. Qiu, T. Shen, K. Yang, and H. Deng, *J. Semicond.* **42**, 112102 (2021).
- [19] L. Zhong, X. Li, W. Wang, and X. Xiao, *J. Semicond.* **44**, 012701 (2023).
- [20] H. Xie, E. S. Bozin, Z. Li, M. Abeykoon, S. Banerjee, J. P. Male, G. J. Snyder, C. Wolverton, S. J. L. Billinge, and M. G. Kanatzidis, *Adv. Mater.* **34**, 2202255 (2022).
- [21] J. Zhang, R. Liu, N. Cheng, Y. Zhang, J. Yang, C. Uher, X. Shi, L. Chen, and W. Zhang, *Adv. Mater.* **26**, 3848 (2014).
- [22] A. Janotti and S.-H. Wei, *Appl. Phys. Lett.* **81**, 3957 (2002).
- [23] H. Xie, Z. Li, Y. Liu, Y. Zhang, C. Uher, V. P. Dravid, C. Wolverton, and M. G. Kanatzidis, *J. Am. Chem. Soc.* **145**, 3211 (2023).
- [24] Y. Cao, X. Su, F. Meng, T. P. Bailey, J. Zhao, H. Xie, J. He, C. Uher, and X. Tang, *Adv. Funct. Mater.* **30**, 2005861 (2020).
- [25] S. Wei and A. Zunger, *J. Appl. Phys.* **78**, 3846 (1995).
- [26] B. Mansour and M. El-Hagary, *Thin Solid Films* **256**, 165 (1995).
- [27] J. K. Furdyna, *J. Appl. Phys.* **64**, R29 (1988).
- [28] S. Shirakata, N. Hapoo, and S. Hosokawa, *Phys. Status Solidi A* **216**, 1800971 (2019).
- [29] Y. Zhong, Y. Luo, X. Li, and J. Cui, *ACS Appl. Energy Mater.* **3**, 12468 (2020).
- [30] R. Wang, B. Dou, Y. Zheng, and S.-H. Wei, *Sci. China-Phys. Mech. Astron.* **65**, 107311 (2022).
- [31] P. Hohenberg and W. Kohn, *Phys. Rev.* **136**, B864 (1964).
- [32] W. Kohn and L. J. Sham, *Phys. Rev.* **140**, A1133 (1965).
- [33] G. Kresse and J. Hafner, *Phys. Rev. B* **47**, 558 (1993).
- [34] G. Kresse and J. Hafner, *Phys. Rev. B* **49**, 14251 (1994).
- [35] G. Kresse and J. Furthmüller, *Phys. Rev. B* **54**, 11169 (1996).
- [36] P. E. Blöchl, *Phys. Rev. B* **50**, 17953 (1994).
- [37] G. Kresse and D. Joubert, *Phys. Rev. B* **59**, 1758 (1999).
- [38] J. Heyd, G. E. Scuseria, and M. Ernzerhof, *J. Chem. Phys.* **118**, 8207 (2003).
- [39] A. Togo and I. Tanaka, *Scr. Mater.* **108**, 1 (2015).
- [40] W. Li, J. Carrete, N. A. Katcho, and N. Mingo, *Comput. Phys. Commun.* **185**, 1747 (2014).
- [41] Z. Han, X. Yang, W. Li, T. Feng, and X. Ruan, *Comput. Phys. Commun.* **270**, 108179 (2022).
- [42] T. J. Scheidemantel, C. Ambrosch-Draxl, T. Thonhauser, J. V. Badding, and J. O. Sofo, *Phys. Rev. B* **68**, 125210 (2003).
- [43] A. Faghaninia, G. Yu, U. Aydemir, M. Wood, W. Chen, G.-M. Rignanese, G. J. Snyder, G. Hautier, and A. Jain, *Phys. Chem. Chem. Phys.* **19**, 6743 (2017).
- [44] A. M. Ganose, J. Park, A. Faghaninia, R. Woods-Robinson, K. A. Persson, and A. Jain, *Nat. Commun.* **12**, 2222 (2021).
- [45] S. Chen, X. G. Gong, A. Walsh, and S.-H. Wei, *Phys. Rev. B* **79**, 165211 (2009).
- [46] J. Ma and S.-H. Wei, *Phys. Rev. Lett.* **110**, 235901 (2013).
- [47] L.-D. Yuan, H.-X. Deng, S.-S. Li, S.-H. Wei, and J.-W. Luo, *Phys. Rev. B* **98**, 245203 (2018).
- [48] K. Yang, H. Yang, Y. Sun, Z. Wei, J. Zhang, P.-H. Tan, J.-W. Luo, S.-S. Li, S.-H. Wei, and H.-X. Deng, *Sci. China-Phys. Mech. Astron.* **66**, 277311 (2023).

- [49] See Supplemental Material at <http://link.aps.org/supplemental/10.1103/PhysRevB.109.035205> for more details on the computational details of phonon dispersion, fourth-order phonon-scattering rates, hole-phonon scattering, the comparison of our results and experimental results, and the density of states.
- [50] S. Huang, Z. Wang, R. Xiong, H. Yu, and J. Shi, *Nano Energy* **62**, 212 (2019).